Is earlier always better? A comparative assessment of rainfall timing for multiyear drought alleviation in China

Yichen Zhang[1], Fubao Sun[2], Wenbin Liu[2], Jie Zhang[1*], Wenli Lai[3], Jiquan Lin[4], Wenchao Sun[5], Wenjie Liu[1], Zhongyi Sun[1], Peng Wang[1]

[1]School of Ecology, Hainan University, Haikou, 570228, China
[2]Key Laboratory of Water Cycle and Related Land Surface Processes, Institute of Geographic Sciences and Natural Resources Research, Chinese Academy of Sciences, Beijing, 100101, China
[3]School of Geography and Environmental Sciences, Hainan Normal University, Haikou, 571158, China
[4]Hainan Provincial Ecological Environment Monitoring Center, Haikou 571126, China
[5]College of Water Sciences, Beijing Normal University, Xinjiekouwai Street 19, Beijing, 100875, China

Corresponding to: Jie Zhang (zhang_jie@hainanu.edu.cn)

Abstract. Multiyear droughts (MYDs) are recognized as severe drought events, with profound impacts on both human activities and ecosystems. However, the timing that maximizes drought attenuation efficiency under additional precipitation ($t_{optimal}$) remains insufficiently quantified. With that in mind, we conducted a retrospective grid-based analysis of historical MYDs in China using the Palmer Drought Severity Index (PDSI) over the full data record of 1961-2020, with a fixed baseline period of 1961-1990. We then performed a series of numerical experiments with hypothetical precipitation gradient increases during the experiment period of 1991-2020 for 351 selected grid-level MYD instances identified across 199 grids ($2° \times 2°$), and developed a drought attenuation quantitative model (DAQM). In addition, a key coefficient (k) derived from DAQM was defined to quantify MYD attenuation efficiency, and $t_{optimal}$ was then determined as the timing at which k reaches its maximum (k_{max}). Overall, drought severity (DS) exhibits a nonlinear response to hypothetical precipitation increases. k_{max} occurred most frequently in the first month of the grid-level drought event (t_1), accounting for 58.79% of all grids, while the second (t_2) and third (t_3) months were also non-negligible, accounting for 22.11% and 11.06%, respectively. Compared to the humid river basins in southern China, the arid and semi-arid northern regions had a higher probability for k at t_2 or t_3 to exceed k at t_1. Drought duration (DD) was identified as a key factor, as longer DD was associated with a greater likelihood of t_2 or t_3 being the $t_{optimal}$, evidenced by R^2 values of 0.526 and 0.578, respectively. These findings provide conceptual guidance for understanding the timing and regional differences in MYD alleviation by clarifying when precipitation inputs are most effective in reducing DS.

1 Introduction

Droughts are recognized as a major natural hazard with profound negative effects on both human activities and the environment (Berdugo et al., 2020; Shi et al., 2021; Palagi et al., 2022). Compared to other natural hazards, droughts often rank higher in key characteristics of losses, such as total loss of life and total economic loss (Mishra and Singh, 2010). For

instance, in the United States, drought caused $250 billion in damages and nearly 3,000 deaths between 1980 and 2020, making it the costliest and second deadliest natural disaster during this period (Ault, 2020; Smith, 2020). In Europe, drought-related financial losses over the three decades prior to 2007 were estimated to exceed EUR 100 billion (Blauhut et al., 2016). In China, prolonged droughts in Southwest China during 2018-2020 resulted in economic losses of $240 million, underscoring the intensifying impacts of prolonged droughts (Feng et al., 2025). Such devastating drought events, which typically last more than 12 months (Brunner and Tallaksen, 2019; Mourik et al., 2025), are referred to as multiyear droughts (MYDs). Under climate change, these persistent, expansive, and difficult-to-recover MYD events have shown an escalating trend in severity, duration, and frequency (Dai, 2013; Zhang et al., 2016; Stevenson et al., 2022; Chen et al., 2025; Wang et al., 2025).

Droughts are primarily related to prolonged reductions in the precipitation for a region (McCabe and Wolock, 2015; Hao et al., 2018; Zhang et al., 2021). For instance, the Millennium Drought in southeast Australia (2001-2009) was the longest drought on record for the region (Van Dijk et al., 2013). Similarly, the California droughts from 2012 to 2015 included the driest three-year period on record in the state (2012-2014) (Mao et al., 2015; Luo et al., 2017). The MYD in Europe from 2014 to 2018 was also record-breaking for the region (Moravec et al., 2021; Büntgen et al., 2021). To better quantify the severity of drought, various drought indices have been developed based on deviations in water availability against long-term normal conditions. Currently, the most widely used drought indices include the Palmer Drought Severity Index (PDSI), Standardized Precipitation Evapotranspiration Index (SPEI), and Standardized Precipitation Index (SPI) (Zhang et al., 2016; Liu et al., 2017; Mukherjee et al., 2021). These indices typically quantify drought severity on a monthly timescale based on precipitation and/or potential evapotranspiration (PET) (Easterling et al., 2007; Vicente-Serrano et al., 2010). They generally standardize monthly effective precipitation time series under the assumption of a normal distribution, enabling the identification of thresholds that delineate different drought intensities (Dai, 2011; Vicente-Serrano et al., 2025). Moreover, by thoughtfully incorporating auto-correlation processes (such as auto-correlation coefficients or the accumulation of antecedent water deficit/surplus), these indices can effectively capture the dynamic evolution of typical drought events, including their onset, development, recovery, and termination (Gupta and Karthikeyan, 2024). To further characterize the dynamic evolution of typical drought events, Yevjevich (1967) proposed the run theory, which extracts drought features based on three key characteristics. These include: (a) Drought duration (DD, the period during which a drought parameter is continuously below the critical threshold), (b) Drought intensity (DI, the maximum deviation of the drought index below the critical threshold during a drought event), (c) Drought severity (DS, the cumulative deficiency of a drought parameter below the critical threshold throughout the event). Such drought event features have been widely applied at station, regional, and global scales to assess drought processes and related impacts (Gu et al., 2020; Wu et al., 2022; Ullah et al., 2022; Zhou et al., 2023), with DS particularly offering a more integrated measure of drought impact (Cavus and Aksoy, 2020).

Previous studies have examined the dynamic evolution of drought events across the four stages, namely onset, development, recovery, and termination (Ma et al., 2023; Lin et al., 2023). It has been widely observed that the recovery and termination phases are often accompanied by increased precipitation (Haile et al., 2020). However, such hydrometeorological changes

typically occur several months after the onset of severe drought, by which time substantial ecological, agricultural, and socioeconomic damages may have already occurred (DeChant and Moradkhani, 2015; Livneh and Hoerling, 2016; Wu et al., 2018). For example, in southeast Australia, the Millennium Drought (2001-2009) was terminated by unusually high rainfall in early 2010, yet this MYD still exhibited prolonged DD and high DS (Yang et al., 2017). Consequently, precipitation occurring earlier in the drought event is more effective in alleviating drought impacts (Fig. 1a and 1b). From another perspective, drought indices typically represent anomalies from normal conditions in a standardized way, allowing comparisons across space and time. This implies that during extreme drought, when the standardized index deviates far from zero, even small increases in precipitation can induce relatively large numerical shifts in the index, owing to the probabilistic structure of standardized indices. In contrast, when the index is closer to zero, the same precipitation perturbation results in much smaller numerical changes. For instance, using the widely applied PDSI as an example, achieving the same one-unit change in the index requires only about 48% of the cumulative probability shift under extreme drought conditions (PDSI = -4) compared with that required under milder drought conditions (PDSI = -1) (Fig. 1c and 1d). This reflects the non-linear probabilistic spacing of the standardized drought indices, whereby values far below the drought threshold are numerically more sensitive to identical perturbations. Consequently, index responses to the same precipitation perturbation can differ substantially depending on the magnitude of PDSI deviations. However, such nonlinear responses are often overlooked. Small increases in precipitation during extreme drought are frequently dismissed as inconsequential, despite their potential to drive meaningful recovery (Pan et al., 2013). Zhang et al. (2024) noted that the effect of a 1% precipitation increase on drought recovery probability under extremely dry conditions is 13.2 times greater than under extremely wet conditions.

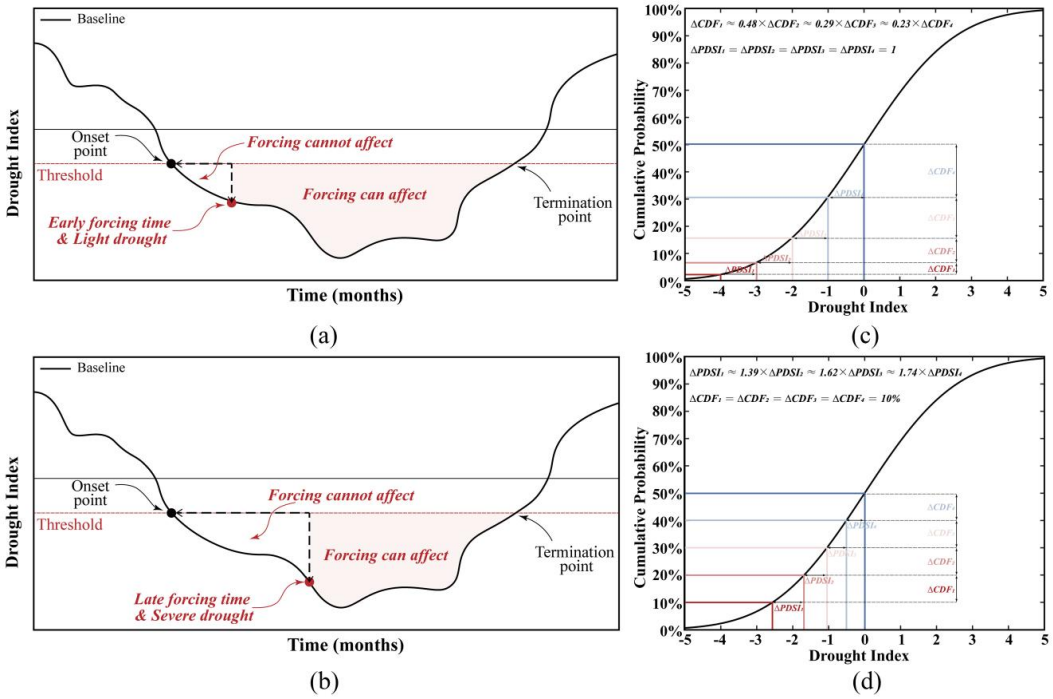


Figure 1: Conceptual and statistical illustrations related to drought alleviation and the normal distribution characteristics of commonly used drought indices (with PDSI as an example). Here, "forcing" refers to a hypothetical incremental water input applied at a given month within a drought event for conceptual illustration. Panels (a) and (b) illustrate the event-level progression of a drought and the associated accumulation of deficit. (a) During the early stage of a drought event, PDSI deviation is relatively small and the accumulated deficit is low. (b) As the drought progresses toward the drought intensity (DI) point, which is defined as the maximum deviation of the index below the critical threshold during the event, the PDSI deviation increases and the accumulated deficit becomes larger. Panels (c) and (d) illustrate the statistical behavior of the standardized index, independent of event-level cumulative deficit. (c) Change in cumulative probability induced by a one-unit shift in PDSI at different levels of PDSI deviation below the drought threshold. (d) PDSI shift required to achieve an equivalent change in cumulative probability at different levels of PDSI deviation.

Currently, the timing that maximizes drought attenuation efficiency under additional precipitation ($t_{optimal}$) remains insufficiently quantified. Several existing studies focus on early drought monitoring or alleviation measures during severe drought (Haile et al., 2020). However, we suggest that effective drought alleviation may not necessarily occur at either of these two stages. In particular, cases where early precipitation input and drought conditions are considered together remain under-investigated. Therefore, it is necessary to clarify the relationship between the timing of precipitation input and drought alleviation. Because MYDs involve cumulative water deficits across seasons and years, exhibiting more persistent impacts, the timing of additional precipitation becomes more critical for alleviation, making MYDs particularly suitable for examining precipitation effects on DS. To this end, we propose a new framework involving a series of numerical experiments to retrospectively investigate typical historical MYD events. In this study, MYD events are defined at the grid level as the basic analytical units, with each representing a temporally continuous drought period identified independently within a single grid. Section 2 introduces the study area and datasets. In Section 3, representative MYD events are identified based on existing literature, with a particular focus on assessing the extent of drought alleviation during these events. A model based on hypothetical precipitation forcing applied at different months of MYD is developed to parameterize MYD attenuation efficiency. The accuracy of this parameter is evaluated by comparing model-derived estimates with empirical estimates derived directly from the numerical experiments. The results and related discussion are presented in section 4 and section 5. We close with a brief conclusion in Section 6.

2 Study area and datasets

To assess the role of nonlinear patterns in MYD alleviation, we utilize a daily meteorological dataset suitable for calculating PDSI during the period of 1961 to 2020 over China. This dataset includes precipitation (pr), air temperature (mean, maximum, and minimum), relative humidity, wind speed, and sunshine duration. This dataset consisting of 756 stations is provided by the National Climate Centre of the China Meteorological Administration and has been quality-controlled before being released to the scientific community (http://www.nmic.gov.cn/). Given the importance of reliable statistics, we applied additional temporal and spatial consistency control on the data based on the information of the length of available data, the missing data, and the density of stations, etc. First, we conducted temporal consistency control on the dataset. Daily records from 1960-2020 were examined for each station, and stations with more than 5% missing values were excluded. Short gaps

(≤5days) in the remaining stations were filled using linear interpolation, while longer gaps were replaced with the multi-year mean for the corresponding day. Following this procedure, 620 out of 756 meteorological stations with continuous measurements were selected. These stations are distributed in 10 large river basins covering China, as shown in Fig. 2. Second, we conduct further control on the spatial inhomogeneity of station distribution. We select 199 grid boxes of 2° × 2° longitude by latitude (Fig. 2), and each grid box should contain at least one station with continuing meteorological measurements. For the given grid box with multiple stations, the station results were averaged to represent the grid box. In doing that, we reduce the possible influence from temporal and spatial inhomogeneities in the data and ensure that the overall statistics are robust. The resulting grid-level daily meteorological series were then used as the basis for subsequent monthly aggregation and PDSI calculation.

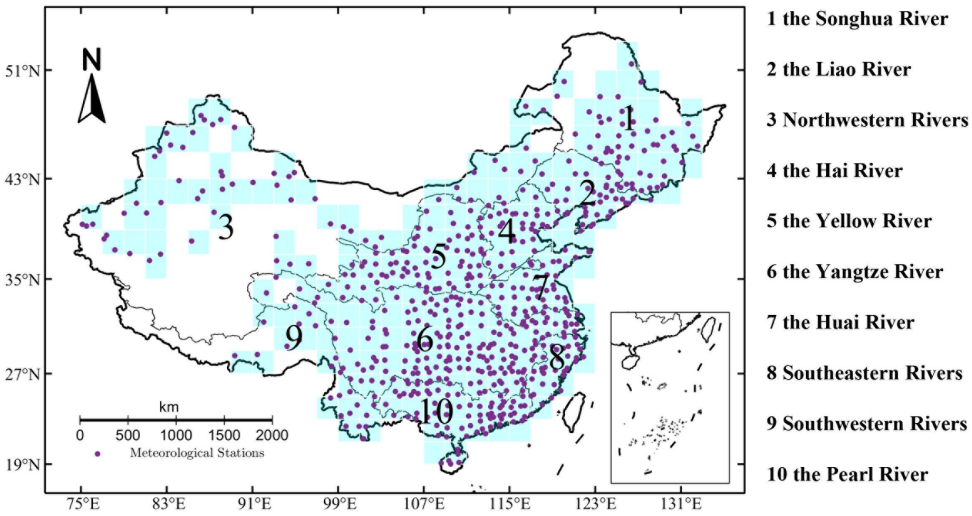


Figure 2: The study area covers 10 large river basins (regions). No. 1, the Songhua River; No. 2, the Liao River; No. 3, Northwestern Rivers; No. 4, the Hai River; No. 5, the Yellow River; No. 6, the Yangtze River; No. 7, the Huai River; No. 8, Southeastern Rivers; No. 9, Southwestern Rivers and No. 10, Pearl River. A total of 199 (2° × 2°) grid boxes (color: cyan) were identified as containing at least one station with continuous instrumental meteorological records. In total, 620 meteorological stations (purple dots) were used.

3 Methods

3.1 Overview

To determine $t_{optimal}$ of drought alleviation, we propose the following methodological framework that evaluates how early-stage hypothetical precipitation forcing and PDSI deviation magnitude jointly modulate the efficiency of alleviating grid-level MYD events. We calculate the PDSI using data from meteorological stations, identify representative grid-level MYD events which capture the key characteristics of persistent and severe droughts, and characterize them in terms of DS, DD, DI,

Drought Development Period (DDP), and Drought Intensity Point (DIP, the PDSI value at the drought intensity point) (see Section 3.3 for identification criteria). Based on these identified grid-level MYDs, a series of numerical experiments is conducted by applying hypothetical precipitation increases along a prescribed gradient. The numerical experiment consists of the following three steps: (1) Validation of the nonlinear response of DS to incremental precipitation forcing applied along a gradient; (2) Construction of a novel drought attenuation quantitative model (DAQM) to describe this response; (3) Verification of the applicability of the key parameter derived from the DAQM, namely k, the MYD attenuation efficiency coefficient. k characterizes how rapidly additional precipitation is converted into reductions in DS. For each grid-level MYD, k is evaluated across different forcing timings, and its maximum value (k_{max}) is identified. The $t_{optimal}$ is then identified as the timing corresponding to k_{max}. In addition, we examine the relationship between DD, as a key event characteristic, and MYD attenuation efficiency under hypothetical precipitation forcing. A detailed description of each methodological component is provided in Sections 3.2-3.4. For clarity, a consolidated table listing principal symbols, acronyms and their description is provided for reference (Table S1 of the Supplement). Figure 3 provides an overview of the workflow and methodological structure of the proposed framework.

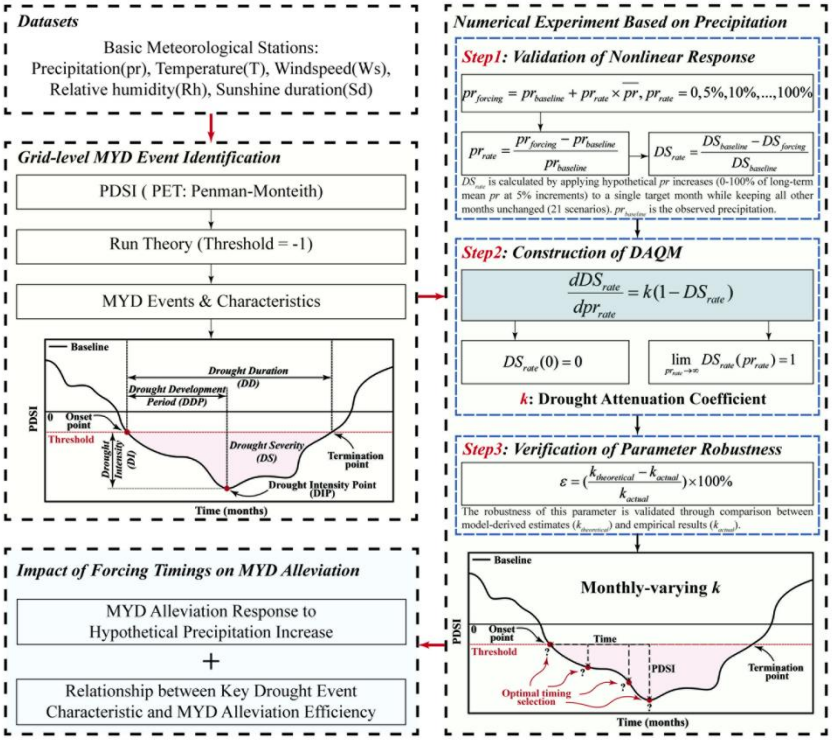


Figure 3: Workflow and method overview.

3.2 Estimation of PDSI using the Penman-Monteith method

In this study, PDSI was used to quantify the deviation between observed monthly precipitation and the required precipitation, which was estimated each month under Climatically Appropriate For Existing Conditions (CAFEC). The PDSI was calculated following the CAFEC formulation and calibrated at the grid level over the baseline period 1961-1990 to calculate CAFEC values and establish a fixed climatological reference. This ensured that PDSI thresholds remained unchanged throughout the analysis. The baseline period was intentionally kept independent from the subsequent numerical experiments, which were conducted exclusively for 1991-2020, in order to avoid altering the reference climatology and to allow consistent evaluation of hypothetical precipitation forcing effects. During the calibration period, monthly climatological values of the water balance components, including precipitation, PET, recharge, runoff, and losses, were derived to compute CAFEC precipitation, calibration coefficients, and the corresponding Z-index and PDSI time series.

The PDSI formulation was based on a simple two-layer water balance model (Palmer, 1965), which considered both water supply and atmospheric evaporative demand. To ensure the credibility of PDSI results, we used the Penman-FAO56 method with a physically based formulation (Xu et al., 2022) to estimate PET (denoted as *PET_pm*), as shown in Eq. (1). Specifically, daily PET was first calculated from daily meteorological observations and then aggregated to monthly values for use in the PDSI calculation.

$$PET_pm = \frac{0.408 \cdot \Delta \cdot (R_n - G) + \gamma \cdot \frac{900}{T + 273} \cdot U_2 \cdot e_s \cdot (1 - Rh/100)}{\Delta + \gamma \cdot (1 + 0.34 \cdot U_2)} \quad (1)$$

Where Δ is the slope of the vapor pressure curve, R_n is the net radiation (calculated using surface downwelling/upwelling shortwave/longwave radiation), G is the soil heat flux, which was assumed to be negligible ($G \approx 0$) at the daily timescale beneath the grass reference surface (Allen et al., 1998), γ is the psychometric constant, T is the monthly averaged air temperature, U_2 is the wind speed at 2m height, e_s is the saturation vapor pressure at a given air temperature, Rh is the relative humidity.

In this study, long-term PDSI series for the period 1961-2020 were calculated using the tool provided by the Palmer Drought Severity Index (Jacobi et al., 2013).

3.3 Identification and characterization of grid-level MYD events based on run theory

Run theory is a threshold-based method that defines drought events as temporally continuous periods during which PDSI remains below -1 (Yang et al., 2024), such that any month exceeding this threshold marks the termination of an event. According to this method, each identified drought event was further characterized using a set of event-based indicators, including DS, DD, DI, DDP, and DIP.

In this study, the identified grid-level drought events were further selected to capture the key characteristics of MYDs that are both persistent and sufficiently severe (hereafter referred to as typical MYDs), by retaining only those with DD>12 and

DI<−3 (Brunner and Tallaksen, 2019; Mourik et al., 2025; Chen et al., 2025). MYDs were required to be temporally continuous, with PDSI remaining below -1 throughout the entire event. Since the calibration period was set to 1961-1990 and the CAFEC values needed to remain fixed during numerical experiments, the final selection was restricted to grid-level MYD samples occurring during 1991-2020. A total of 351 grid-level MYD samples meeting these criteria were identified. Each basin contained at least 11 grid-level MYD samples, thereby helping to ensure the statistical robustness of the analysis.

3.4 Numerical experiment design for quantifying drought attenuation efficiency under hypothetical precipitation increase

According to run theory, for a given drought event characterized by its baseline monthly PDSI series (Fig. 4a), a hypothetical precipitation increase applied at a specific month leads to a reduction in DS, assuming all other conditions remain unchanged. This provides a foundation for quantifying drought attenuation efficiency in terms of DS reduction. The numerical experiments therefore apply hypothetical precipitation increases to individual months of a drought event independently, keeping all other months unchanged, and compare the resulting DS responses across months. The timing of hypothetical precipitation increases ($t_{forcing}$) is a key experimental parameter, representing the month at which the additional precipitation is applied within a grid-level MYD event.

Two conceptual models are proposed to characterize different patterns of drought attenuation efficiency. Conceptual Model 1 considers the same hypothetical precipitation increase applied at different $t_{forcing}$ within an MYD event (Fig. 4b). Because the precipitation perturbation can influence DS only from $t_{forcing}$ onward, an earlier $t_{forcing}$ allows a longer period during which the drought process can be affected. Consequently, $t_{optimal}$ under Conceptual Model 1 occurs at the beginning of the event (t_1), i.e., $t_{optimal} \rightarrow t_1$. Conceptual Model 2 features the same precipitation forcing applied at the same $t_{forcing}$, but under different PDSI values (Fig. 4c). As a standardized index, PDSI exhibits tail sensitivity, whereby values further below the drought threshold tend to experience larger numerical responses under identical precipitation perturbations. Because DS is calculated as the cumulative sum of monthly PDSI values over DD, this property of PDSI also affects event-level DS. This property of PDSI underlies Conceptual Model 2, linking the single-month PDSI response to the event-level DS response and providing a mechanistic basis for interpreting attenuation efficiency from this perspective. Therefore, $t_{optimal}$ under Conceptual Model 2 tends to coincide with the month of DIP occurrence (t_{DIP}), i.e., $t_{optimal} \rightarrow t_{DIP}$. To determine a composite $t_{optimal}$ that integrates patterns described in both Conceptual Model 1 and Conceptual Model 2, we designed a series of numerical experiments involving precipitation gradient increases at different $t_{forcing}$ (Fig. 4d). This composite $t_{optimal}$ represents the primary target of this study. Because the $t_{optimal}$ under the combined patterns remains undetermined, it is essential to first define a plausible time range in which it may occur. Given that the t_{DIP} of MYD events typically occurs much later than the onset ($t_{DIP} \gg t_1$), the $t_{optimal}$ is expected to fall within the interval from t_1 to t_{DIP}.

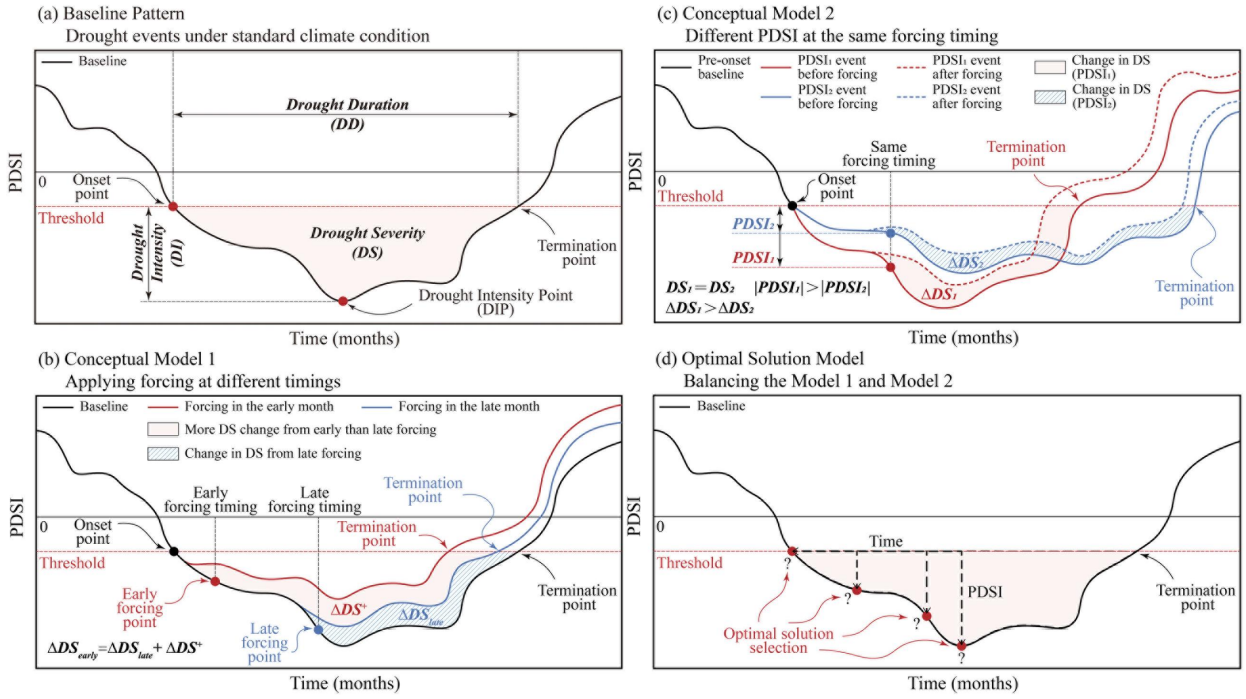


Figure 4: Conceptual models illustrating MYD alleviation driven by hypothetical increased precipitation forcing: (a) Baseline pattern without increased forcing. *DS* is represented by the area of the red region. (b) Conceptual model 1: The same hypothetical precipitation increase applied at different $t_{forcing}$ within an MYD event. An earlier $t_{forcing}$ leads to greater alleviation benefits (ΔDS^+, red area) and avoids additional losses from cumulative precipitation deficits. (c) Conceptual model 2: The same hypothetical precipitation increase applied at the same $t_{forcing}$, but with different drought index values. Because standardized drought indices exhibit tail sensitivity, deeper drought conditions tend to produce large DS reductions under identical forcing ($\Delta DS_1 > \Delta DS_2$). (d) Optimal solution model: By weighing the mismatch influences of hypothetical precipitation forcing described in Conceptual models 1 and 2, $t_{optimal}$ (marked by the red point) can be identified.

Since this study focuses on drought alleviation, only hypothetical precipitation increase scenarios with incremental gradients are considered. The procedures of this numerical experiment were given as follows:

Step 1: Validation of nonlinear response

To validate the nonlinear response of MYD alleviation to hypothetical precipitation increases applied at different $t_{forcing}$ and under varying PDSI values, a single-timing precipitation forcing strategy was adopted. Under this strategy, precipitation is increased at only one $t_{forcing}$ within an MYD event, while precipitation in all other months remains unchanged. Since the baseline scenario in this study corresponds to the period 1961-1990, all numerical experiments were conducted for MYDs occurring after 1990, with no temporal overlap between the two periods. This design ensures that the reference climate is not influenced by hypothetical precipitation perturbations. Consequently, the baseline remains fixed throughout all gradient-based numerical experiments. The forcing strategy for a given MYD event during 1991-2020 is expressed as follows:

$$pr_{forcing} = pr_{baseline} + pr_{rate} \times \overline{pr},\ pr_{rate} = 0,\ 5\%,\ 10\%,\ \ldots,\ 100\% \quad (2)$$

Where $pr_{forcing}$ is the precipitation in the targeted month after applying the hypothetical forcing, $pr_{baseline}$ is the observed precipitation in the same month under the baseline (unforced) scenario, pr_{rate} is a dimensionless proportion (0–1) controlling the relative magnitude of the hypothetical precipitation addition, $\overline{pr}$ is the long-term mean monthly precipitation, and $pr_{rate} \times \overline{pr}$ is the imposed hypothetical precipitation increment.

As described above, applying precipitation forcing alters the DS of the corresponding MYD event. Therefore, the relationship between $pr_{forcing}$ and the resulting change in DS provides a basis for examining the nonlinear response of drought alleviation to hypothetical precipitation increases.

Step 2: Construction of DAQM

To further parameterize drought attenuation efficiency in a consistent and comparable way across grids, forcing timings and MYDs, we developed DAQM. DAQM describes the relationship between hypothetical precipitation perturbations and the resulting reductions in event-level DS. It provides a unified framework for estimating the attenuation efficiency coefficient (k) while accounting for the nonlinear responses implied by Conceptual Models 1 and 2.

DS is defined as the cumulative sum of PDSI values over DD of a grid-level MYD period. In the model formulation, attenuation of DS under hypothetical precipitation increases is represented as a nonlinear diminishing-return process. This functional form is motivated by numerical experiments, which consistently show that incremental precipitation inputs produce progressively smaller marginal reductions in DS across grids and forcing timings, indicating a bounded drought alleviation response.

To represent this behavior, we adopt a first-order kinetic-like formulation, in which the instantaneous rate of DS reduction is proportional to the remaining DS. This structure captures rapid initial alleviation when residual DS is high and progressively slower alleviation as DS approaches zero.

Accordingly, Eq. (3) expresses the drought attenuation process in differential form, linking the instantaneous rate of DS reduction to the residual DS:

$$\frac{\partial DS_{rate}}{\partial pr_{rate}} = k \cdot (1 - DS_{rate}) \quad (3)$$

Where DS_{rate} ($= \frac{DS_{baseline} - DS_{forcing}}{DS_{baseline}}$, $DS_{baseline}$ is the observed *DS* under the baseline scenario, and $DS_{forcing}$ is the *DS* after the hypothetical precipitation is applied) is the relative change in *DS*.

k is the attenuation efficiency coefficient, representing the proportionality with which additional precipitation is converted into reductions in residual *DS*.

It is clear that when no hypothetical precipitation forcing is applied (pr_{rate}=0), there is no change in DS ($DS_{rate} = 0$). Likewise, when sufficient forcing is applied, the MYD is fully alleviated ($DS_{rate} = 1$). Thus, the model is subject to the following boundary and limiting conditions:

$$\begin{cases} DS_{rate}(0) = 0 & (4) \\ \lim_{pr_{rate}\to\infty} DS_{rate}(pr_{rate}) = 1 & (5) \end{cases}$$

Thus, based on the differential equation 3 above and the boundary and limiting conditions in equations 4 and 5, the analytical solution describing the relationship between DS_{rate} and pr_{rate} can be obtained as follows:

$$DS_{rate} = 1 - exp(-k \cdot pr_{rate}) \quad (6)$$

To ensure that this exponential structure reflects observed system behavior rather than an assumed mathematical form, we compared formulations inspired by zero-order, first-order, and second-order kinetic processes using historical MYDs during 1991-2020. Across most grids and events, the first-order structure more accurately reproduced the curvature observed in the numerical experiments (Table S2 of the supplement). Extension to an n-order formulation showed that the estimated n converged toward unity (n≈0.98), further supporting the first-order representation. We also compared the exponential form against alternative empirical relationships. Logistic curves did not match the observed pattern. Power-law functions were unable to satisfy the required boundary conditions.

Step 3: Verification of parameter robustness

To evaluate the robustness of the drought attenuation efficiency parameter *k*, we compared model-derived estimates obtained from DAQM ($k_{theoretical}$) with empirical estimates calculated directly from the numerical experiments (k_{actual}). Specifically, $k_{theoretical}$ is obtained by fitting the DAQM analytical solution to the full set of experimental outcomes, thereby capturing the nonlinear and bounded response of DS to hypothetical precipitation increases. In contrast, k_{actual} represents the empirical sensitivity of DS to small precipitation perturbations and is approximated from the initial slope of the relationship between DS_{rate} and pr_{rate} under the smallest forcing step ($k_{actual}=\frac{DS_{rate}(pr_{rate}=0.05)}{0.05}$, where 0.05 is the smallest perturbation step used in the experiments).

The relative error between $k_{theoretical}$ and k_{actual} was used as a diagnostic measure to assess the numerical reliability of the model-based parameterization:

$$\varepsilon = \left(\frac{k_{theoretical} - k_{actual}}{k_{actual}}\right) \times 100\% \qquad (7)$$

Where ε is the relative error, $k_{theoretical}$ is the model-derived attenuation efficiency coefficient, and k_{actual} is the empirical estimate obtained from numerical experiments.

In subsequent analyses, $k_{theoretical}$ is used as the primary indicator because it captures the overall nonlinear response structure of DS to hypothetical precipitation increases and provides a more comprehensive and comparable measure of drought attenuation efficiency across grids and forcing timings. k_{actual} is employed solely to verify internal consistency and is not used in other analyses.

4 Results

4.1 Response relationship between DS and hypothetical precipitation increase in China

Focusing on drought alleviation, the numerical experiments were constrained to the $t_{forcing}$ range of DDP, with the minimum DDP among the selected MYD events being 8 months. Accordingly, t_1, t_2, ..., and t_8, represent the first to the eighth month of MYD. For each $t_{forcing}$ from t_1 to t_8, DS_{rate} values were calculated across hypothetical precipitation perturbations with pr_{rate} ranging from 0 to 1 at 0.05 increments. The resulting responses were then fitted using the DAQM analytical form described in Section 3.4 (Eq. (6)). Fig. 5 presents the resulting DAQM fitted curves, derived from median DS_{rate} responses calculated for each pr_{rate} first across events within each grid and then across grids within the study region. The fitted curves closely reproduced the numerical experiment outputs with R^2 values exceeding 0.90 for all eight curves, confirming the suitability of the DAQM analytical form. This fitting yields one theoretical attenuation efficiency parameter (k) for each $t_{forcing}$, representing the overall drought attenuation efficiency under different drought conditions. The corresponding k values are denoted as k_1, k_2, ..., and k_8, respectively.

The changes in DS are not proportional along the increasing precipitation gradient. Within the same pr_{rate} range from 0 to 1, all timings from t_1 to t_8 exhibited a similar nonlinear diminishing-return response pattern. However, the maximum DS_{rate} (at $pr_{rate} = 1$) indicated that the most effective MYD attenuation occurred during t_1 to t_3 (Fig. 5). The values of maximum DS_{rate} in the response curves for t_1 to t_3 were 0.60, 0.59, and 0.57, respectively. Correspondingly, the fitted k values for t_1 to t_3 were 0.92, 0.88, and 0.84, respectively. This result reflects the influence of Conceptual Model 1 as discussed in Section 3.4 (Fig. 4b), in which earlier hypothetical precipitation forcing provides greater potential for DS reduction.

To illustrate the full nonlinear attenuation response pattern, DS_{rate} responses were evaluated across the full precipitation forcing range. Because drought conditions correspond to PDSI values below the drought threshold ($PDSI<-1$), the magnitude of deviation below the threshold was used to facilitate clearer comparisons. As shown in Fig. 5, the drought attenuation process can be divided into five stages based on a gradual increase in pr_{rate} from 0 to 1 (i.e., 0-0.2, 0.2-0.4, 0.4-

0.6, 0.6-0.8, and 0.8-1.0). In the first stage, when pr_{rate} increases from 0 to 0.2, the magnitude of deviation below the drought threshold at pr_{rate} = 0.2 is smaller than that at pr_{rate} = 0, indicating drought alleviation. In the second stage, as pr_{rate} increases from 0.2 to 0.4, the reduced deviation reached at the end of the first stage (i.e., weaker drought conditions) serves as the new starting point for this stage. Consequently, the deviation at the beginning of the second stage is already smaller than that in the first stage, and the same pattern applies to subsequent stages. According to Conceptual Model 2 described in Section 3.4 (Fig. 4c), even when the increment in pr_{rate} is the same across two stages, a smaller magnitude of deviation below the drought threshold at the beginning of the stage (i.e., weaker drought conditions) leads to a smaller increase in DS_{rate} (Fig. 5). This explains the nonlinear response pattern observed between DS_{rate} and pr_{rate} ($\frac{d(DS_{rate})}{d(pr_{rate})} > 0, \frac{d^2(DS_{rate})}{d(pr_{rate})^2} < 0$) shown in Fig. 5. For instance, the efficiency decline at t_1 is illustrated by the blue shaded area in Fig. 5.

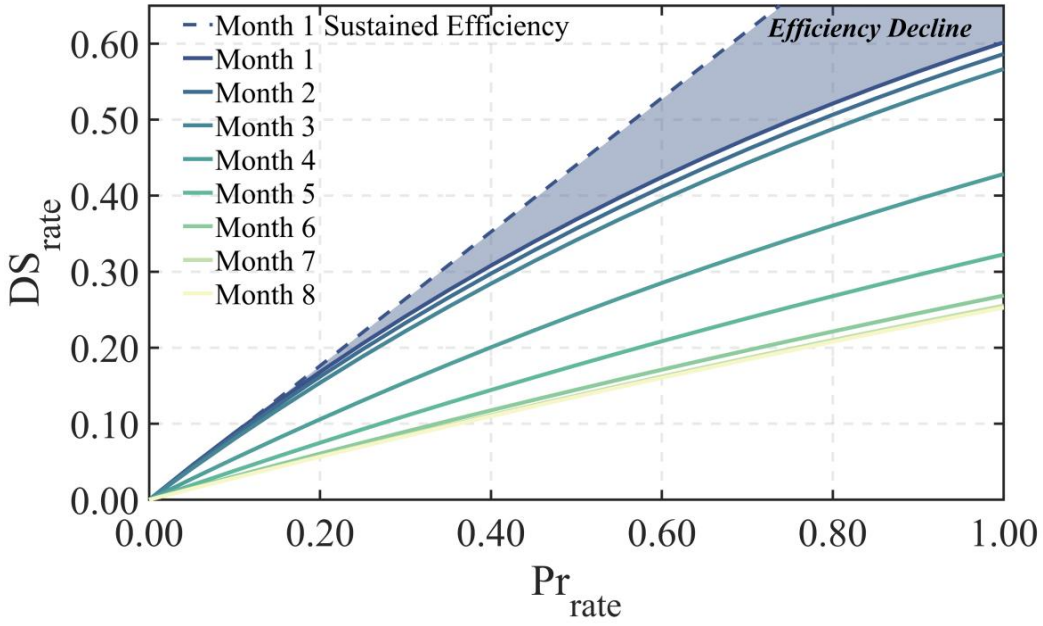


Figure 5: Nonlinear response of DS to hypothetical precipitation during DDP in China. The blue area indicates the decline in MYD attenuation efficiency at t_1 due to the nonlinear response of DS to hypothetical precipitation, relative to the idealized linear response (i.e., the sustained efficiency scenario).

4.2 Validation of the MYD attenuation efficiency coefficient in China

According to the DAQM constructed in Section 3.4, as the increment in pr_{rate} approaches zero, the corresponding DS_{rate} also approaches zero. Under this condition, the estimated value of k approaches the actual k. In other words, the actual k can be approximated using a small value of pr_{rate} (such as pr_{rate} = 0.05) and its corresponding DS_{rate}. Therefore, we calculated the actual values of k based on the DS_{rate} at pr_{rate} = 0.05. These actual values were then compared with the theoretical k values derived from the DAQM developed in Section 3.4, at the grid scale. The comparison helped to validate the applicability of the theoretical model under varying spatial conditions. Fig. 6a shows the spatial distribution of ε across all given grids, with 72.86% exhibiting a ε below 5%. This high consistency suggests that the theoretical model provides reliable estimates of drought attenuation efficiency across diverse regions. Some spatial variation in relative error can be observed across different hydro-climatic conditions. Slightly higher relative errors appear in some arid river basins in northern China, which may be attributed to the strong influence of evaporative demand on drought variability in these regions rather than precipitation alone. Since the numerical experiment perturbs only hypothetical precipitation while keeping PET fixed, the influence of non-precipitation drivers may be reflected in the estimate of k. In contrast, relatively higher errors in some humid river basins in southern China are mainly due to the high baseline precipitation. Under such conditions, the minimum experimental increment (pr_{rate} = 0.05) represents a relatively large increase in water input, which leads to a greater deviation from the initial slope represented by k_{actual}. In semi-arid river basins, precipitation remains the dominant driver of drought development. In these regions, the experimental increment represents a modest perturbation relative to baseline precipitation, leading to the strongest agreement between theoretical and actual estimates. Despite these regional differences, relative errors remain modest overall (mostly around 6%), confirming the robustness of the theoretical model across regions.

For each grid, the k_{max} (corresponding to the value of k at $t_{optimal}$) value was first identified. Fig. 6b then illustrates the spatial pattern of the corresponding $t_{forcing}$ at which the k_{max} occurs across the study area. Generally, t_1 dominates, accounting for 58.79% of the grids. Nonetheless, t_2 and t_3 are also non-negligible, representing 22.11% and 11.06%, respectively. Accordingly, we further investigate these timing-related spatial variations at the basin scale. Overall, a strong positive correlation was observed between the theoretical and actual values, with R^2 values exceeding 0.90 for t_1, t_2, and t_3 across the ten river basins in China (Fig. 6c-e). The comparison results for each month revealed no significant deviation from the 1:1 reference line, with slopes of 1.063, 1.060, and 1.037 for t_1, t_2, and t_3, respectively (Fig. 6c-e).

These results demonstrate the robustness and applicability of the theoretical values at both the grid and river basin scales. For this reason, the DAQM was further employed to investigate drought attenuation efficiency at different $t_{forcing}$. Particular attention was given to how this efficiency varies when insights from Conceptual Model 1 and Conceptual Model 2 are jointly considered. This quantitative model was also used to identify $t_{optimal}$ for precipitation input across t_1, t_2, and t_3.

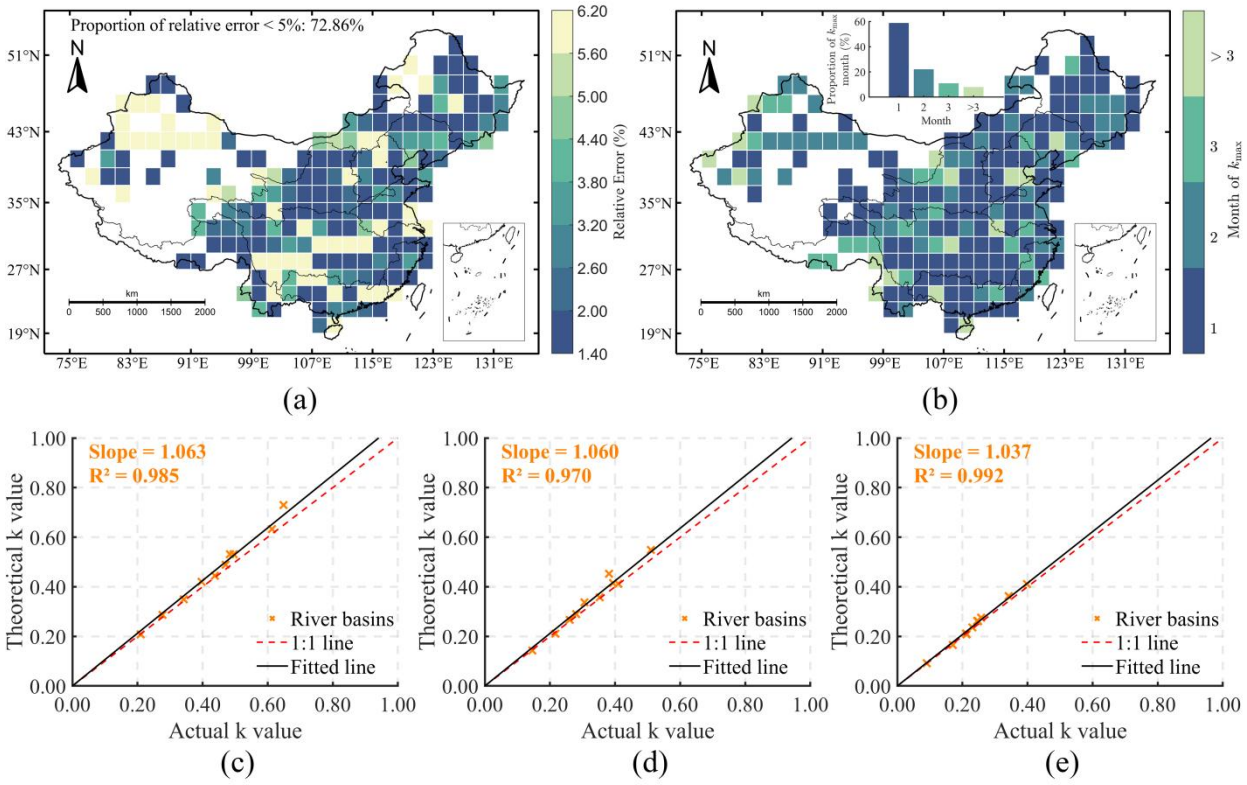


Figure 6: Verification of the applicability of *k*. (a) Spatial distribution of ε for each grid. (b) Spatial distribution of the timing at which the k_{max} occurs in each grid. The inset shows the frequency histogram of the timings of k_{max} values across all grids. (c-e) Median actual versus median theoretical *k* values for the ten major river basins in (c) t_1, (d) t_2, and (e) t_3. The red dashed line is the 1:1 line. The black solid line is the fitted line based on values from 10 river basins. Orange crosses are the values for individual river basins.

4.3 Quantification of the relationship between MYD attenuation efficiency and precipitation input timing in China

To identify $t_{optimal}$ in various river basins during t_1, t_2, and t_3, a series of numerical experiments were conducted using the DAQM. Fig. 7 presents the spatial distributions of the changes in k between t_2 and t_1 ($\Delta k_{21} = k_2 - k_1$), and between t_3 and t_1 ($\Delta k_{31} = k_3 - k_1$). As demonstrated by the validation results shown in Fig. 6, the theoretical model performs robustly across most regions. Therefore, the spatial patterns shown in Fig. 7 can be considered reliable for interpreting drought attenuation efficiency. To enable a clearer comparison of magnitude among cases where $\Delta k < 0$, absolute values were used. Notably, the larger absolute values of negative Δk ($\Delta k < 0$) were mainly observed in the humid river basins of southern China, particularly in the Pearl River and Yangtze River basins (Fig. 7 and Table 1). By comparison, smaller absolute values of negative Δk were detected in the arid and semi-arid northern regions of China, particularly in the Liao River basin (Fig. 7 and Table 1). Moreover, in 118 out of 199 grids (59.30%), the absolute values of negative Δk_{31} were larger than those of Δk_{21} (Fig. 7 and Table 1). This disparity indicates that, in most occurrences of MYD, the greatest attenuation efficiency

occurs during the early stage of MYD events, as described in Conceptual Model 1 in Section 3.4 (Fig. 4b). Meanwhile, as shown in Fig. 7, we found that 74 out of 199 grids (37.19%) exhibited at least one positive value in either Δk_{21} or Δk_{31}. These results indicate that, in a non-negligible portion of grids, the greatest attenuation efficiency does not occur at t_1, as described in Conceptual Model 2 in Section 3.4 (Fig. 4c).

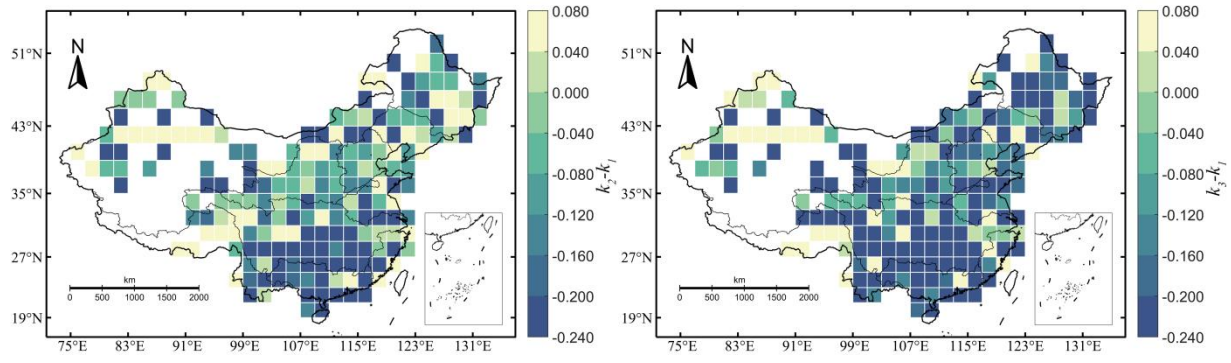
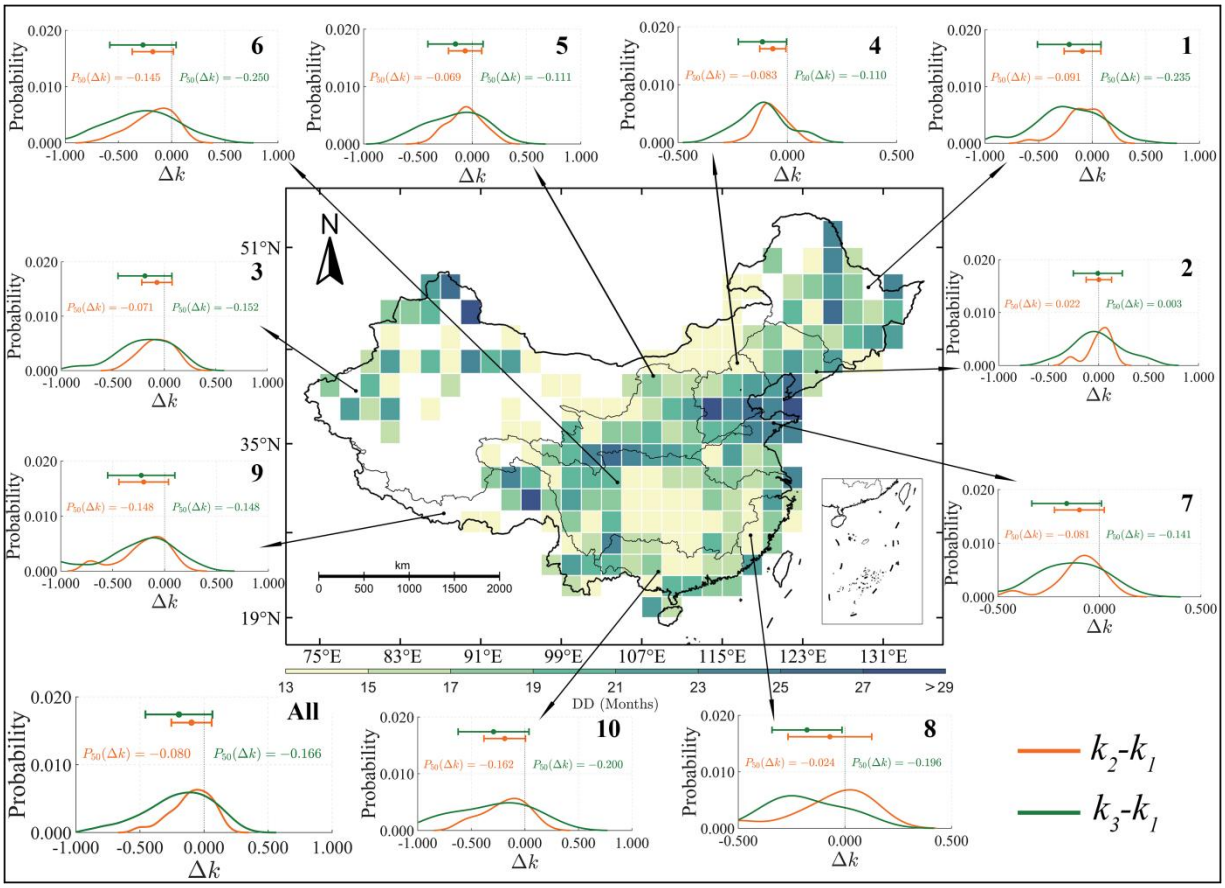


Figure 7: Spatial distribution of the changes in k (Δk). (a) Change in k between t_2 and t_1 (Δk_{21}). (b) Change in k between t_3 and t_1 (Δk_{31}).

These experiments also aimed to identify the key drought event characteristics responsible for the variation in $t_{forcing}$. Since DS represents the cumulative water deficit over the entire DD, and k is derived from DS, DD constitutes an important factor influencing k in addition to the standardized characteristics of PDSI itself. Therefore, the spatial distribution and statistical characteristics of DD are examined to help interpret basin-scale differences in k (Fig. 8 and Table 1). We summarize the probability density function (PDF) of Δk_{21}, and Δk_{31} for all of grid-level MYD events across 10 river basins in China (Fig. 8 and Table 1). The Δk values exhibit a roughly normal distribution across river basins (Fig. 8). The median values of both Δk_{21} and Δk_{31} are negative in 9 out of 10 basins, with the median of Δk_{31} being lower than that of Δk_{21} (Table 1). In most basins, the standard deviation of Δk_{31} is also larger than that of Δk_{21}, indicating greater variability in the efficiency difference between t_3 and t_1 (Fig. 8). These results suggest that the efficiency advantage of early precipitation input ($t_1 > t_2$ and $t_1 > t_3$). As emphasized by Conceptual Model 1, earlier drought alleviation yields greater effectiveness. This advantage becomes more pronounced when comparing t_1 and t_3. However, positive Δk_{21} and Δk_{31} values were found in 33.67% and 23.12% of all grids, respectively (Fig. 7a and 7b). Similar results were also evident in the PDFs for all of China and each individual basin (Fig. 8). These results suggest the non-negligible role of Conceptual Model 2. Longer DD tends to be associated with Δk values closer to or even above zero (Fig. 8 and Table 1). In particular, the Liao River, with a relatively long DD of 28 months ($DD_{all\ China} = 21\ months$), shows median Δk values of 0.022 for Δk_{21} and 0.003 for Δk_{31} (Fig. 8 and Table 1). In contrast, the Pearl River, characterized by a shorter DD of 19 months, exhibits more negative median Δk values of -0.162 and -0.200 for Δk_{21} and Δk_{31} (Fig. 8 and Table 1), respectively.



400

Figure 8: Spatial distribution of the median drought duration from 1991 to 2020 across the 10 river basins in China. Surrounding panels show the probability distribution of Δk for all of China and each basin, derived from grid-level MYD samples. Specifically, the orange lines represent Δk_{21}, and the green lines represent Δk_{31}. The *x-axis* in each panel denotes Δk, while the *y-axis* denotes probability. The number in the upper-right corner of each panel indicates the basin code.

405

410

Table 1: Summary of the number of grids, median values of DD and Δk, including $\Delta k_{21}(=k_2-k_1)$, $\Delta k_{31}(=k_3-k_1)$, and $\Delta k_{32}(=k_3-k_2)$, across the ten river basins and all of China.

River basin	Number of grids	Median DD (Months)	$P_{50}(\Delta k_{21})$	$P_{50}(\Delta k_{31})$	$P_{50}(\Delta k_{32})$
Songhua River	26	22	-0.091	-0.235	***-0.142***
Liao River	10	28	**0.022**	**0.003**	**-0.024**
Northwestern Rivers	44	17	-0.071	-0.152	-0.087
Hai River	8	29	-0.083	-0.110	-0.053
Yellow River	20	21	-0.069	-0.111	-0.090
Yangtze River	39	19	-0.145	***-0.250***	-0.127
Huai River	11	23	-0.081	-0.141	-0.042
Southeastern Rivers	8	14	-0.024	-0.196	-0.077
Southwestern Rivers	15	21	-0.148	-0.148	-0.083
Pearl River	18	19	***-0.162***	-0.200	-0.063
All of China	199	21	-0.080	-0.166	-0.094

Note: The bold value marks the maximum P_{50} among the ten river basins in China, and the bold-italic value marks the minimum P_{50}.

To further investigate the influence of DD as an important event characteristic, an equal-width binning method was applied to examine the variation of Δk under different DD values. Specifically, the original DD values of the selected MYD events ranged from 13 to 51 months. These events were grouped into bins according to their DD values. To ensure the robustness of the results (each bin contained no fewer than 10 grid-level events), the DD range was limited to 13 to 40 months, and the bin width was set to 4 months. This setting yielded a total of seven bins (Fig. 9). We calculated the median values of both Δk and DD within each bin. As shown in Fig. 9, we found a positive correlation between DD and Δk, with R^2 values of 0.526 and 0.578 for Δk_{21} and Δk_{31}, respectively. Notably, when DD exceeds 29 months (as shown in Fig. 9), the Δk values approaching zero, indicating that the drought attenuation efficiencies of t_2 and t_3 become comparable to that of t_1. In contrast, when DD is shorter (around 17 months, as shown in Fig. 9), t_1 demonstrates notably higher drought attenuation efficiency than t_2 and t_3. These results suggest that DD is a key factor influencing $t_{optimal}$.

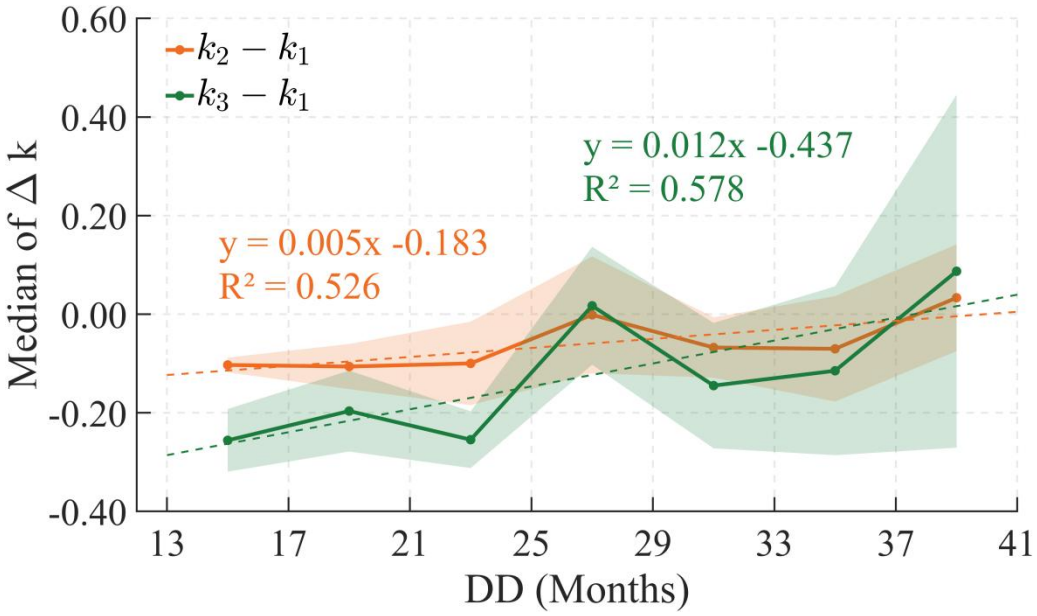


Figure 9: Median Δk of MYD under different DD. The orange line represents Δk_{21}, and the green line represents Δk_{31}. Shaded areas indicate half the standard error as the confidence interval.

To clarify the alleviation advantages of the composite $t_{optimal}$ (defined in Section 3.4), both Conceptual Model 1 and Conceptual Model 2 (as discussed in Section 3.4) were considered. Fig. 10 and Table 2 present a comparison between the drought attenuation efficiency of $t_{optimal}$ and those of t_1 and t_{DIP} (defined in Section 3.4). The corresponding k at t_1 (k_1), t_{DIP} (k_{DIP}), and $t_{optimal}$ (k_{max}) exhibit differences. For simplicity, we define two ratios, k_{max}/k_1 and k_{max}/k_{DIP}, to quantify the differences in k between $t_{optimal}$ and t_1, and between $t_{optimal}$ and t_{DIP}, respectively. In terms of magnitude, k_{max}/k_1 is typically close to 1, while k_{max}/k_{DIP} consistently exceeds 2 (Table 2). From the perspective of Conceptual Model 1, t_1 tends to dominate (Fig. 10a and Table 2). Nevertheless, the presence of grids with $k_{max}/k_1 > 1$ suggests $t_{optimal} > 1$ should not be overlooked (Fig. 10a). At the basin scale, t_1 dominates in most regions, except in the Liao River basin, where the median k_{max}/k_1 reaches 1.135 (Table 2). In contrast, the comparison with Conceptual Model 2 suggests that $t_{optimal}$ offers a more substantial advantage in drought attenuation efficiency compared to t_{DIP} (Fig. 10b and Table 2). This advantage is particularly pronounced in the Liao River and Songhua River basins, where the median k_{max}/k_{DIP} values reach 15.430 and 12.555, respectively. By contrast, the advantage of $t_{optimal}$ is less evident in the Southeastern River and Hai River basins, with median k_{max}/k_{DIP} values of 3.428 and 2.413, respectively.

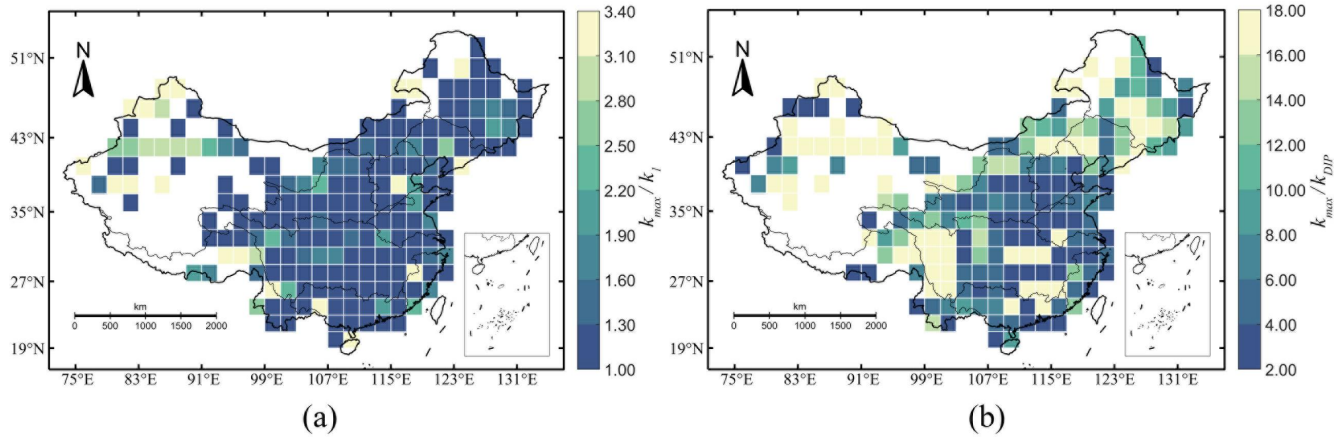


Figure 10: Spatial distribution of the ratios of k derived from the Optimal Solution Model relative to those derived separately from Conceptual Model 1 and Conceptual Model 2. (a) The ratio of k between the $t_{optimal}$ and t_1 (k_{max}/k_1), (b) the ratio of k between the $t_{optimal}$ and t_{DIP} (k_{max}/k_{DIP}).

Table 2: Summary of the median values of k_{max}/k_1 and k_{max}/k_{DIP} across the ten river basins and all of China.

River basin	*P50* (k_{max}/k_1)	*P50* (k_{max}/k_{DIP})
Songhua River	1.000	12.555
Liao River	**1.135**	**15.430**
Northwestern Rivers	1.023	7.677
Hai River	1.000	***2.413***
Yellow River	1.001	4.932
Yangtze River	1.000	4.704
Huai River	1.000	3.707
Southeastern Rivers	1.000	3.428
Southwestern Rivers	1.069	6.539
Pearl River	1.000	3.429
All of China	1.000	6.979

Note: The bold value marks the maximum P_{50} among the ten river basins in China, and the bold-italic value marks the minimum P_{50}.

5 Discussion

5.1 MYD alleviation response to hypothetical increased precipitation

Current studies on precipitation-based drought alleviation, referring to the dominant role of precipitation in driving drought alleviation, have primarily focused on the early stage of drought development (DeChant and Moradkhani, 2015; Livneh and Hoerling, 2016; Wu et al., 2018). Yang et al. (2017) integrated early precipitation input with drought-induced losses and concluded that earlier precipitation is more effective in alleviating drought impacts. This is consistent with the discussion of Conceptual Model 1 in Section 3.4. However, due to the statistical properties of standardized drought indices, more severe drought conditions are often associated with higher attenuation efficiency under increased precipitation (Fig. 1). Zhang et al. (2024) highlighted that extremely dry conditions tend to exhibit a higher probability of drought recovery under the same level of increased precipitation. This finding can be explained by Conceptual Model 2 presented in Section 3.4. The nonlinear pattern in DS response to increased precipitation (Fig. 1 and Fig. 5) can be more comprehensively understood by jointly considering these two conceptual models. To further clarify this relationship, we derived response curves at different $t_{forcing}$ (Fig. 5) based on the DAQM developed in Section 3.4. Under the same hypothetical precipitation forcing, a higher value of k at a given $t_{forcing}$ indicates greater drought attenuation efficiency. Our findings reveal that the $t_{optimal}$ of MYD ranges from t_1 to t_{DIP} (Fig. 10 and Table 2).

Consistent with several existing studies (Pan et al., 2013; Haile et al., 2020), t_1 remains the dominant $t_{optimal}$ across China. However, we noted that t_2 and t_3, while occurring later than t_1, are still non-negligible in the early stage of MYD. Spatially, the grids where t_2 and t_3 are dominant account for 22.11% and 11.06% of all grids, respectively (Fig. 6b). According to the classification of climate zones based on average annual precipitation (Yang et al., 2022), compared with the humid river basins in southern China, the arid and semi-arid northern regions exhibited a higher probability that drought attenuation efficiency at t_2 and t_3 exceeds that at t_1 (Fig. 7 and Fig. 10a). This interpretation is supported by the strong agreement between theoretical and actual k values shown in Fig. 6. We noticed that the Liao River basin (semi-arid basin) and Pearl River basin (humid basin) exhibited relatively high and low MYD attenuation efficiency, respectively. This may be attributed to the generally more severe drought conditions in the Liao River basin compared to those in the Pearl River basin (Huang et al., 2019; Lai et al., 2024; Zhang et al., 2025). Due to the characteristics of standardized drought indices (as discussed in Sections 1 and 3.4), increased precipitation tends to be more effective in alleviating drought impacts in the Liao River basin. This conclusion was consistent with previous findings (Zhang et al., 2024; Wang et al., 2025), showing the importance of earlier precipitation input for alleviating MYD in the humid basins of China. In a word, understanding MYD alleviation responses to increased precipitation is essential for guiding more targeted and effective drought alleviation strategies, ensuring that interventions are both timely and regionally appropriate.

Although derived from index-based analysis and based on idealized numerical experiments, the identified $t_{optimal}$ may be interpreted as the timing when precipitation input is most efficiently converted into overall drought alleviation, thereby providing a temporal reference for water allocation decisions. $t_{optimal}$ can be conceptually associated with a sensitive phrase

within drought propagation. As this timing represents the highest precipitation responsiveness during a MYD, identifying $t_{optimal}$ clarifies when the system can achieve the greatest alleviation advantage prior to later stages of drought evolution. Improvements realized at this timing provide a more favorable initial condition for subsequent hydrological and ecological adjustments.

5.2 Key drought event characteristics influencing MYD attenuation efficiency

Recent studies have shown that droughts are increasing in both frequency and severity (Dai, et al., 2020; Fischer, et al., 2025; Gebrechorkos, et al., 2025), although substantial regional differences exist. Similarly, Chen et al. (2025) highlighted that MYDs are also becoming more frequent and severe at global scales. To further characterize the dynamic evolution of MYD, three commonly used features include DD, DS, and DI. Among these, DD is a key factor for identifying MYDs, as MYDs are typically defined by a duration exceeding 12 months (Massari et al., 2022). DS represents the overall impact of MYD, while DI is related to the onset timing of the recovery stage. In current studies, standardized drought indices are commonly used to quantify drought severity (Mishra and Singh, 2010). According to the statistical characteristics of the normal distribution (Dai, 2011), drought indices responses to identical precipitation inputs can vary considerably depending on the magnitude of index values below the drought threshold. This aligns with Conceptual Model 2 presented in Section 3.4, where small increases in precipitation have the potential to induce substantial shifts toward alleviation when the index deviates far below the drought threshold. Our findings further indicate that t_1 and t_{DIP} of MYD do not coincide, especially in longer-duration MYD, where t_{DIP} tends to occur much later than t_1. With that in mind, we examined the relationship between DD and *k*. Our results demonstrate a positive correlation between DD and *k* in MYD (Fig. 8 and Fig. 9). Specifically, basins in northern China, characterized by longer DD, tend to have a higher probability of t_2 or t_3 being the $t_{optimal}$ in contrast to southern basins with shorter DD (Fig. 8 and Table 1).

5.3 Limitations and uncertainties

Droughts are not only influenced by *pr*, but also by other non-precipitation factors such as wind speed, air temperature, radiation, and relative humidity, among others. These non-precipitation factors are widely used to estimate potential evapotranspiration (Gebrechorkos et al., 2025). However, this study focuses solely on *pr*. This is primarily because drought alleviation mainly depends on the effective management and allocation of available water resources. In future studies, the performance of the framework could be further enhanced by considering these non-precipitation factors. It is essential to recognize that our study is a retrospective analysis based on historical MYDs. This study provides a framework for identifying $t_{optimal}$ at the early stage of MYD development in drought early warning systems. However, determining whether a drought event would develop into an MYD at an early stage remains a major challenge (Xu et al., 2021; Gumus, 2023). This challenge arises from the complexity of the factors influencing the development of droughts into MYDs. Furthermore, this study currently focuses solely on meteorological drought. Research on other types of drought, such as agricultural, hydrological, and socio-economic droughts, will also be a key focus in future studies. Future research should evaluate the

applicability of our framework to other types of drought. To this end, it is also necessary to further optimize the framework by fully considering additional influencing factors (Tian et al., 2022; Wu et al., 2022; Meresa et al., 2023).

6 Conclusion

This study applied a series of numerical experiments involving hypothetical precipitation gradient increases to investigate $t_{optimal}$ of drought alleviation for 351 historical MYDs during 1991-2020 across ten river basins in China, based on monthly PDSI calculated from daily meteorological data. Following these experiments, we developed the DAQM, a single-parameter model designed to quantify drought attenuation efficiency through the key coefficient, k, with $t_{optimal}$ identified as the timing corresponding to k_{max}. The main conclusions can be summarized as follows:

(1) We revealed a nonlinear response relationship between DS and hypothetical precipitation forcing applied incrementally along a gradient. This nonlinear response is well characterized by the DAQM, as shown by close alignment between model-derived and empirical estimates (slopes of 1.063, 1.060, and 1.037 for t_1, t_2, and t_3 along the 1:1 reference line), confirming its reliability in quantifying drought attenuation efficiency.

(2) While t_1 remains the dominant $t_{optimal}$ in most regions, accounting for 58.79% of all grids, t_2 and t_3 are also non-negligible, accounting for 22.11% and 11.06%, respectively. These findings indicate that although precipitation input during t_1 is generally more effective in reducing drought severity, a non-negligible portion of grids suggest that t_1 is not always optimal, and precipitation input during t_2 or t_3 may lead to greater drought alleviation under certain conditions. Compared to the humid river basins in Southern China, the arid and semi-arid northern regions exhibited a higher probability that the k at t_2 or t_3 would exceed that at t_1.

(3) DD is a key factor for determining $t_{optimal}$ for drought alleviation, as MYDs are typically defined by a duration exceeding 12 months. Longer DD was associated with a greater likelihood of t_2 or t_3 being the $t_{optimal}$, evidenced by R^2 values of 0.526 and 0.578, respectively. When DD exceeds 29 months, the MYD attenuation efficiencies of t_2 and t_3 become comparable to that of t_1.

With the increasing frequency and severity of MYDs in the future, our findings can offer conceptual and methodological guidance for developing more targeted and effective alleviation strategies by considering the timing of precipitation input across regions.

Code availability

All MATLAB codes can be provided by the corresponding authors upon request.

Data availability

The daily meteorological dataset from 756 stations suitable for calculating PDSI during the period of 1961 to 2020 over China is available from the National Meteorological Information Center of the China Meteorological Administration via http://www.nmic.cn/.

Author contributions

YZ: Conceptualization, Data curation, Formal analysis, Funding acquisition, Investigation, Methodology, Supervision, Validation, Visualization, Writing - original draft, Writing - review and editing. **FS**: Conceptualization, Investigation, Methodology, Supervision, Writing - review and editing. **WBL**: Conceptualization, Investigation, Formal analysis, Methodology, Validation, Writing - review and editing. **JZ**: Conceptualization, Formal analysis, Funding acquisition, Investigation, Methodology, Project administration, Resources, Supervision, Validation, Writing - review and editing. **WLL**: Data curation, Investigation, Methodology, Project administration, Supervision. **JL**: Data curation, Investigation, Validation, Visualization. **WS**: Conceptualization, Formal analysis, Methodology. **WJL**: Conceptualization, Methodology, Project administration. **ZS**: Data curation, Visualization. **PW**: Formal analysis, Validation.

Competing interests

The authors declare that they have no conflict of interest.

Acknowledgments

The authors express their gratitude to the National Natural Science Foundation of China, Hainan Province Science and Technology Special Fund, and the Innovative Research Projects for Postgraduates of Hainan Province for the financial support of this research project.

Financial support

This research has been supported by the National Natural Science Foundation of China (grant Nos. 41901043 and 42261005); Hainan Province Science and Technology Special Fund (grant No. ZDYF2023SHFZ092); and the Innovative Research Projects for Postgraduates of Hainan Province (grant No. Qhyb2024-100).

References

Allen, R. G., Pereira, L. S., Raes, D., and Smith, M.: FAO Irrigation and Drainage Paper No. 56 – Crop Evapotranspiration, FAO, Rome, Italy, 1998.

Ault, T.R.: On the essentials of drought in a changing climate, Science, 368, 256-260, doi: 10.1126/science.aaz5492, 2020.

Berdugo, M., Delgado-Baquerizo, M., Soliveres, S., Hernández-Clemente, R., Zhao, Y., Gaitán, J.J., Gross, N., Saiz, H., Maire, V., Lehmann, A., and Rillig, M.C.: Global ecosystem thresholds driven by aridity, Science, 367, 787-790, doi: 10.1126/science.aay5958, 2020.

Blauhut, V., Stahl, K., Stagge, J.H., Tallaksen, L.M., De Stefano, L., and Vogt, J.: Estimating drought risk across Europe from reported drought impacts, drought indices, and vulnerability factors, Hydrol. Earth Syst. Sci., 20 , 2779-2800, doi: https://doi.org/10.5194/hess-20-2779-2016, 2016.

Brunner, M.I. and Tallaksen, L.M.: Proneness of European catchments to multiyear streamflow droughts, Water Resour. Res., 55, 8881-8894, doi: https://doi.org/10.1029/2019WR025903, 2019.

Büntgen, U., Urban, O., Krusic, P.J., Rybníček, M., Kolář, T., Kyncl, T., Ač, A., Koňasová, E., Čáslavský, J., Esper, J., and Wagner, S.: Recent European drought extremes beyond Common Era background variability, Nat. Geosci., 14, 190-196, doi: https://doi.org/10.1038/s41561-021-00698-0, 2021.

Cavus, Y. and Aksoy, H.: Critical drought severity/intensity-duration-frequency curves based on precipitation deficit, J. Hydrol., 584, 124312, doi: https://doi.org/10.1016/j.jhydrol.2019.124312, 2020.

Chen, L., Brun, P., Buri, P., Fatichi, S., Gessler, A., McCarthy, M.J., Pellicciotti, F., Stocker, B. and Karger, D.N.: Global increase in the occurrence and impact of multiyear droughts, Science, 387, 278-284, doi: 10.1126/science.ado4245, 2025.

Dai, A.: Drought under global warming: a review, Wiley Interdiscip. Rev., 2, 45-65, doi: https://doi.org/10.1002/wcc.81, 2011.

Dai, A.: Increasing drought under global warming in observations and models, Nat. Clim. Change, 3, 52-58, doi: https://doi.org/10.1038/nclimate1633, 2013.

Dai, M., Huang, S., Huang, Q., Leng, G., Guo, Y., Wang, L., Fang, W., Li, P., and Zheng, X.: Assessing agricultural drought risk and its dynamic evolution characteristics, Agric. Water Manage., 231, 106003, doi: https://doi.org/10.1016/j.agwat.2020.106003, 2020.

DeChant, C.M. and Moradkhani, H.: Analyzing the sensitivity of drought recovery forecasts to land surface initial conditions, J. Hydrol., 526, 89-100, doi: https://doi.org/10.1016/j.jhydrol.2014.10.021, 2015.

Easterling, D.R., Wallis, T.W., Lawrimore, J.H., and Heim Jr, R.R.: Effects of temperature and precipitation trends on US drought, Geophys. Res. Lett., 34, L20709, doi: https://doi.org/10.1029/2007GL031541, 2007.

Feng, X., Wang, Z., Wu, X., Huang, S., Li, J., Lai, C., Zeng, Z., and Lin, G.: Tracking 3D drought events across global river basins: Climatology, spatial footprint, and temporal changes, Geophys. Res. Lett., 52, e2024GL111442, doi: https://doi.org/10.1029/2024GL111442, 2025.

Fischer, E.M., Bador, M., Huser, R., Kendon, E.J., Robinson, A., and Sippel, S.: Record-breaking extremes in a warming climate, Nat. Rev. Earth Environ., 6, 456-470, doi: https://doi.org/10.1038/s43017-025-00681-y, 2025.

Gebrechorkos, S.H., Sheffield, J., Vicente-Serrano, S.M., Funk, C., Miralles, D.G., Peng, J., Dyer, E., Talib, J., Beck, H.E., Singer, M.B., and Dadson, S.J.: Warming accelerates global drought severity, Nature, 642, 628-635, doi: https://doi.org/10.1038/s41586-025-09047-2, 2025.

Gu, L., Chen, J., Yin, J., Sullivan, S.C., Wang, H.M., Guo, S., Zhang, L., and Kim, J.S.: Projected increases in magnitude and socioeconomic exposure of global droughts in 1.5 and 2 °C warmer climates, Hydrol. Earth Syst. Sci., 24, 451-472, doi: https://doi.org/10.5194/hess-24-451-2020, 2020.

Gumus, V.: Evaluating the effect of the SPI and SPEI methods on drought monitoring over Turkey, J. Hydrol., 626, 130386, doi: https://doi.org/10.1016/j.jhydrol.2023.130386, 2023.

Gupta, A. and Karthikeyan, L.: Role of initial conditions and meteorological drought in soil moisture drought propagation: An event-based causal analysis over South Asia, Earth's Future, 12, e2024EF004674, doi: https://doi.org/10.1029/2024EF004674, 2024.

Haile, G.G., Tang, Q., Li, W., Liu, X., and Zhang, X.: Drought: Progress in broadening its understanding, Wiley Interdiscip. Rev.-Water, 7, e1407, doi: https://doi.org/10.1002/wat2.1407, 2020.

Hao, Z., Singh, V.P., and Xia, Y.: Seasonal drought prediction: Advances, challenges, and future prospects, Rev. Geophys., 56, 108-141, doi: https://doi.org/10.1002/2016RG000549, 2018.

Huang, S., Wang, L., Wang, H., Huang, Q., Leng, G., Fang, W., and Zhang, Y.: Spatio-temporal characteristics of drought structure across China using an integrated drought index, Agric. Water Manage., 218, 182-192, doi: https://doi.org/10.1016/j.agwat.2019.03.053, 2019.

Jacobi, J., Perrone, D., Duncan, L.L., and Hornberger, G.: A tool for calculating the Palmer drought indices, Water Resour. Res., 49, 6086-6089, doi: https://doi.org/10.1002/wrcr.20342, 2013.

Lai, C., Sun, H., Wu, X., Li, J., Wang, Z., Tong, H., and Feng, J.: Water availability may not constrain vegetation growth in Northern Hemisphere, Agric. Water Manage., 291, 108649, doi: https://doi.org/10.1016/j.agwat.2023.108649, 2024.

Lin, H., Yu, Z., Chen, X., Gu, H., Ju, Q., and Shen, T.: Spatial-temporal dynamics of meteorological and soil moisture drought on the Tibetan Plateau: Trend, response, and propagation process, J. Hydrol., 626, 130211, doi: https://doi.org/10.1016/j.jhydrol.2023.130211, 2023.

Liu, Y., Zhu, Y., Ren, L., Singh, V.P., Yang, X., and Yuan, F.: A multiscalar Palmer drought severity index, Geophys. Res. Lett., 44, 6850-6858, doi: https://doi.org/10.1002/2017GL073871, 2017.

Livneh, B. and Hoerling, M.P.: The physics of drought in the US central Great Plains, J. Clim., 29, 6783-6804, doi: https://doi.org/10.1175/JCLI-D-15-0697.1, 2016.

Luo, L., Apps, D., Arcand, S., Xu, H., Pan, M., and Hoerling, M.: Contribution of temperature and precipitation anomalies to the California drought during 2012–2015, Geophys. Res. Lett., 44, 3184-3192, doi: https://doi.org/10.1002/2016GL072027, 2017.

Ma, Q., Li, Y., Liu, F., Feng, H., Biswas, A., and Zhang, Q.: SPEI and multi-threshold run theory based drought analysis using multi-source products in China, J. Hydrol., 616, 128737, doi: https://doi.org/10.1016/j.jhydrol.2022.128737, 2023.

Mao, Y., Nijssen, B., and Lettenmaier, D.P.: Is climate change implicated in the 2013–2014 California drought? A hydrologic perspective, Geophys. Res. Lett., 42, 2805-2813, doi: https://doi.org/10.1002/2015GL063456, 2015.

Massari, C., Avanzi, F., Bruno, G., Gabellani, S., Penna, D., and Camici, S.: Evaporation enhancement drives the European water-budget deficit during multi-year droughts, Hydrol. Earth Syst. Sci., 26, 1527-1543, doi: https://doi.org/10.5194/hess-26-1527-2022, 2022.

McCabe, G.J. and Wolock, D.M.: Variability and trends in global drought, Earth Space Sci., 2, 223-228, doi: https://doi.org/10.1002/2015EA000100, 2015.

Meresa, H., Zhang, Y., Tian, J., and Faiz, M.A.: Understanding the role of catchment and climate characteristics in the propagation of meteorological to hydrological drought, J. Hydrol., 617, 128967, doi: https://doi.org/10.1016/j.jhydrol.2022.128967, 2023.

Mishra, A.K. and Singh, V.P.: A review of drought concepts, J. Hydrol., 391, 202-216, doi: https://doi.org/10.1016/j.jhydrol.2010.07.012, 2010.

Moravec, V., Markonis, Y., Rakovec, O., Svoboda, M., Trnka, M., Kumar, R., and Hanel, M.: Europe under multi-year droughts: how severe was the 2014–2018 drought period?, Environ. Res. Lett., 16, 034062, doi: 10.1088/1748-9326/abe828, 2021.

Mukherjee, S. and Mishra, A.K.: Increase in compound drought and heatwaves in a warming world, Geophys. Res. Lett., 48, e2020GL090617, doi: https://doi.org/10.1029/2020GL090617, 2021.

Palagi, E., Coronese, M., Lamperti, F., and Roventini, A.: Climate change and the nonlinear impact of precipitation anomalies on income inequality, Proc. Natl. Acad. Sci., 119, e2203595119, doi: https://doi.org/10.1073/pnas.2203595119, 2022.

Palmer, W.C.: Meteorological drought, Research paper no. 45, US Weather Bureau, Washington, DC, 58 pp., 1965.

Pan, M., Yuan, X., and Wood, E.F.: A probabilistic framework for assessing drought recovery, Geophys. Res. Lett., 40, 3637-3642, doi: https://doi.org/10.1002/grl.50728, 2013.

Shi, H., Tian, H., Lange, S., Yang, J., Pan, S., Fu, B., and Reyer, C.P.: Terrestrial biodiversity threatened by increasing global aridity velocity under high-level warming, Proc. Natl. Acad. Sci., 118, e2015552118, doi: https://doi.org/10.1073/pnas.2015552118, 2021.

Smith, A. B.: 2010-2019: A landmark decade of U.S. billion-dollar weather and climate disasters, National Oceanic and Atmospheric Administration, 2020.

Stevenson, S., Coats, S., Touma, D., Cole, J., Lehner, F., Fasullo, J., and Otto-Bliesner, B.: Twenty-first century hydroclimate: A continually changing baseline, with more frequent extremes, Proc. Natl. Acad. Sci., 119, e2108124119, doi: https://doi.org/10.1073/pnas.2108124119, 2022.

Tian, Q., Lu, J., and Chen, X.: A novel comprehensive agricultural drought index reflecting time lag of soil moisture to meteorology: A case study in the Yangtze River basin, China, Catena, 209, 105804, doi: https://doi.org/10.1016/j.catena.2021.105804, 2022.

Ullah, I., Ma, X., Asfaw, T.G., Yin, J., Iyakaremye, V., Saleem, F., Xing, Y., Azam, K., and Syed, S.: Projected changes in increased drought risks over South Asia under a warmer climate, Earth's Future, 10, e2022EF002830, doi: https://doi.org/10.1029/2022EF002830, 2022.

Van Dijk, A.I., Beck, H.E., Crosbie, R.S., De Jeu, R.A., Liu, Y.Y., Podger, G.M., Timbal, B., and Viney, N.R.: The Millennium Drought in southeast Australia (2001–2009): Natural and human causes and implications for water resources, ecosystems, economy, and society, Water Resour. Res., 49, 1040-1057, doi: https://doi.org/10.1002/wrcr.20123, 2013.

van Mourik, J., Ruijsch, D., van der Wiel, K., Hazeleger, W., and Wanders, N.: Regional drivers and characteristics of multi-year droughts, Weather Clim. Extremes, 48, 100748, doi: https://doi.org/10.1016/j.wace.2025.100748, 2025.

Vicente-Serrano, S.M., Domínguez-Castro, F., Beguería, S., El Kenawy, A., Gimeno-Sotelo, L., Franquesa, M., Azorin-Molina, C., Andres-Martin, M., and Halifa-Marín, A.: Atmospheric drought indices in future projections, Nat. Water., 3, 374-387, doi: https://doi.org/10.1038/s44221-025-00416-9, 2025.

Vicente-Serrano, S.M., Beguería, S., and López-Moreno, J.I.: A multiscalar drought index sensitive to global warming: the standardized precipitation evapotranspiration index, J. Clim., 23, 1696-1718, doi: https://doi.org/10.1175/2009JCLI2909.1, 2010.

Wang, C., Chen, J., Lee, S.C., Xiong, L., Su, T., Lin, Q., and Xu, C.Y.: Response and recovery times of vegetation productivity under drought stress: Dominant factors and relationships, J. Hydrol., 655, 132945, doi: https://doi.org/10.1016/j.jhydrol.2025.132945, 2025.

Wu, J., Chen, X., Yao, H., Liu, Z., and Zhang, D.: Hydrological drought instantaneous propagation speed based on the variable motion relationship of speed-time process, Water Resour. Res., 54, 9549-9565, doi: https://doi.org/10.1029/2018WR023120, 2018.

Wu, J., Yao, H., Chen, X., Wang, G., Bai, X., and Zhang, D.: A framework for assessing compound drought events from a drought propagation perspective, J. Hydrol., 604, 127228, doi: https://doi.org/10.1016/j.jhydrol.2021.127228, 2022.

Wu, W., Zhang, J., Sun, Z., Yu, J., Liu, W., Yu, R., and Wang, P.: Attribution analysis of land degradation in Hainan Island based on geographical detector, Ecol. Ind., 141, 109119, doi: https://doi.org/10.1016/j.ecolind.2022.109119, 2022.

Xu, L., Chen, N., Yang, C., Zhang, C., and Yu, H.: A parametric multivariate drought index for drought monitoring and assessment under climate change, Agric. For. Meteorol., 310, 108657, doi: https://doi.org/10.1016/j.agrformet.2021.108657, 2021.

Xu, Y., Zhu, X., Cheng, X., Gun, Z., Lin, J., Zhao, J., Yao, L., and Zhou, C.: Drought assessment of China in 2002–2017 based on a comprehensive drought index, Agric. For. Meteorol., 319, 108922, doi: https://doi.org/10.1016/j.agrformet.2022.108922, 2022.

Yang, L., Zhao, G., Tian, P., Mu, X., Tian, X., Feng, J., and Bai, Y.: Runoff changes in the major river basins of China and their responses to potential driving forces, J. Hydrol., 607, 127536, doi: https://doi.org/10.1016/j.jhydrol.2022.127536, 2022.

Yang, X., Wu, F., Yuan, S., Ren, L., Sheffield, J., Fang, X., Jiang, S., and Liu, Y.: Quantifying the impact of human activities on hydrological drought and drought propagation in China using the PCR-GLOBWB v2. 0 model, Water Resour. Res., 60, e2023WR035443, doi: https://doi.org/10.1029/2023WR035443, 2024.

Yang, Y., McVicar, T.R., Donohue, R.J., Zhang, Y., Roderick, M.L., Chiew, F.H., Zhang, L., and Zhang, J.: Lags in hydrologic recovery following an extreme drought: Assessing the roles of climate and catchment characteristics, Water Resour. Res., 53, 4821-4837, doi: https://doi.org/10.1002/2017WR020683, 2017.

Yevjevich, V.M.: An objective approach to definitions and investigations of continental hydrologic droughts. Hydro. Pap., Colorado State University, no. 23, 25 pp., 1967.

Zhang, J., Sun, F., Xu, J., Chen, Y., Sang, Y.F., and Liu, C.: Dependence of trends in and sensitivity of drought over China (1961–2013) on potential evaporation model, Geophys. Res. Lett., 43, 206-213, doi: https://doi.org/10.1002/2015GL067473, 2016.

Zhang, L., Yuan, F., and He, X.: Probabilistic assessment of global drought recovery and its response to precipitation changes, Geophys. Res. Lett., 51, e2023GL106067, doi: https://doi.org/10.1029/2023GL106067, 2024.

Zhang, Q., Miao, C., Su, J., Gou, J., Hu, J., Zhao, X., and Xu, Y.: A new high-resolution multi-drought-index dataset for mainland China, Earth Syst. Sci. Data, 17, 837-853, doi: https://doi.org/10.5194/essd-17-837-2025, 2025.

Zhang, W., Furtado, K., Wu, P., Zhou, T., Chadwick, R., Marzin, C., Rostron, J., and Sexton, D.: Increasing precipitation variability on daily-to-multiyear time scales in a warmer world, Sci. Adv., 7, eabf8021, doi: 10.1126/sciadv.abf8021, 2021.

Zhou, Z., Zhang, L., Chen, J., She, D., Wang, G., Zhang, Q., Xia, J., and Zhang, Y.: Projecting global drought risk under various SSP-RCP scenarios, Earth's Future, 11, e2022EF003420, doi: https://doi.org/10.1029/2022EF003420, 2023.